Multiscale time-domain time-lapse FWI with a model-difference regularization

Musa Maharramov, Ganglin Chen, Partha S. Routh, Anatoly I. Baumstein, Sunwoong Lee, and Spyros K. Lazaratos*
ExxonMobil Upstream Research Company

SUMMARY

We present a multiscale time-lapse full-waveform inversion (4D FWI) technique based on a cascaded time-domain simultaneous inversion of multiple surveys with a model-difference regularization. In our cascaded approach, different model scales are recovered using different objective functions and regularization penalties. We apply our method to a synthetic example, and demonstrate a robust recovery of production-induced velocity changes in the presence of repeatability issues and errors in the amplitude information.

INTRODUCTION

Most of the existing time-lapse seismic inversion techniques rely on extracting time shifts and amplitude differences either directly from baseline and monitor surveys or from migrated baseline and monitor image gathers, and converting them into subsurface model changes (Johnston, 2013). This approach is the mainstay of prevalent industry time-lapse practices, and requires a significant amount of survey cross-equalization and manual intervention. Our objective is to automate time-lapse analysis, reducing the amount of interpretation and quality control associated with a typical time-lapse survey. Some existing model and image-space techniques lend themselves to automation but have their own constraints. For example, techniques based on time-lapse wave-equation velocity analysis (WEMVA) (Shragge and Lumley, 2013) inherit resolution limitations of conventional WEMVA, while those based on image-space tomography (Maharramov and Albertin, 2007; Girard and Vasconcelos, 2010) or mixed data-image space methods (Qu and Verschuur, 2016) still require data cross-equalization.

4D FWI, on the other hand, avoids extraction of time-lapse information directly from data or image differences, takes advantage of the high-resolution power of FWI, and can use wide-offset seismic acquisitions in an automated inversion of production-induced model differences (Routh et al., 2012; Zheng et al., 2011; Asnaashari et al., 2012; Raknes et al., 2013; Maharramov and Biondi, 2014; Yang et al., 2014; Maharramov et al., 2015; Willemsen and Malcolm, 2015; Alemie and Sacchi, 2016; Maharramov et al., 2016). Time-lapse FWI (with the exception of double-difference FWI), as a model-space technique, can be less sensitive to survey repeatability issues because direct manipulation of the baseline and monitor data, such as extraction of time displacements, is avoided. In practice, however, differences in survey acquisition parameters and coverage result in inversion artifacts that propagate into the inverted model difference (Asnaashari et al., 2012). Simultaneous inversion of multiple survey vintages in a linearized-waveform inversion (Ayeni, 2011; Ayeni and Biondi, 2012) or full-waveform inversion (Maharramov and Biondi, 2014) was proposed to mitigate this sensitivity, while model-difference regularization (Maharramov and Biondi, 2014) is specifically intended for penalizing artifacts in the model difference. A total-variation (TV) model-difference regularization is useful for the recovery of "blocky" model changes in a tomographic 4D FWI (Maharramov et al., 2015, 2016), while an L_1-based model-difference regularization helps to recover isolated "spiky" anomalies, and can be applied in a cascaded fashion after the inversion with a TV regularization (Maharramov and Biondi, 2017).

In this work we extend the frequency-domain 4D FWI technique of Maharramov et al. (2016) to time domain, and propose a cascaded inversion work flow using alternative objective functions and regularization penalties.

THEORY

We simultaneously invert baseline and monitor models m_1 and m_2 by solving the following optimization problem:

$$\alpha \left\| \frac{u_1}{\|u_1\|} - \frac{d_1}{\|d_1\|} \right\|^2 + \beta \left\| \frac{u_2}{\|u_2\|} - \frac{d_2}{\|d_2\|} \right\|^2 + \tag{1}$$

$$\delta \left\| \mathbf{R}(m_2 - m_1 - \Delta m_0) \right\|_1, \tag{2}$$

where d_1 and d_2 denote the observed baseline and monitor data, u_1 and u_2 are the predicted baseline and monitor data, α, β and δ are misfit and regularization weights, Δm_0 is either a model difference inverted at an earlier stage of the inversion, or a model-difference prior, and $\mathbf{R}$ can be either the identity operator or the spatial gradient operator, $\mathbf{R} = \nabla$. The data misfit terms in Equation 1 are computed for each trace, then summed up for all source and receiver pairs. We have chosen the normalized L_2 misfit function (Routh et al., 2011) because of its reduced sensitivity to amplitude errors in the data or forward modeling. At the first stage of our cascaded inversion we recover "blocky" velocity differences by minimizing the objective function in Equations 1 and 2 with $\mathbf{R} = \nabla$ and $\Delta m_0 = 0$, effectively conducting a simultaneous 4D FWI with a TV regularization of the model difference (Maharramov et al., 2016). At the second stage, we recover "spiky" velocity anomalies by first setting Δm_0 to the model-difference result of the first inversion, then minimizing the objective function in Equations 1 and 2 with the operator $\mathbf{R}$ equal to the identity operator. In some situations our approximation to a "tomographic" inversion using the normalized L_2 may not be sufficiently sensitive to spiky anomalies in the model difference, as is the case with thin reservoirs and coarse computational grids. In such applications, the second stage of the inversion may use the standard L_2 data misfit function,

$$\alpha \left\| u_1 - d_1 \right\|^2 + \beta \left\| u_2 - d_2 \right\|^2 + \tag{3}$$

$$\delta \left\| m_2 - m_1 - \Delta m_0 \right\|_1, \tag{4}$$

thus making the inversion more sensitive to amplitude effects (Maharramov et al., 2016).

EXAMPLES

We generated synthetic data using acoustic modeling with density. The true baseline velocity model used in our experiments is shown in Figure 1, the difference between the monitor and baseline is shown in the zoomed-in Figure 2. The true density model and model difference are obtained from the true velocity model and model difference by dividing them by 1500 (setting water density to 1).

The true velocity difference of Figure 2 was designed to imitate three large 30 m-thick reservoir compartments, and three smaller compartments located up-dip from a partially permeable fault. Velocity changes of -300, -200 and 150 m/s are prescribed in the large compartments to model the effect of gas coming out of the solution (Johnston, 2013) and water substitution (in the lowest compartment). The three small compartments have only negative velocity changes of -200, -100, and -50 m/s to model the effect of gas migrating up-dip through the partially conductive fault.

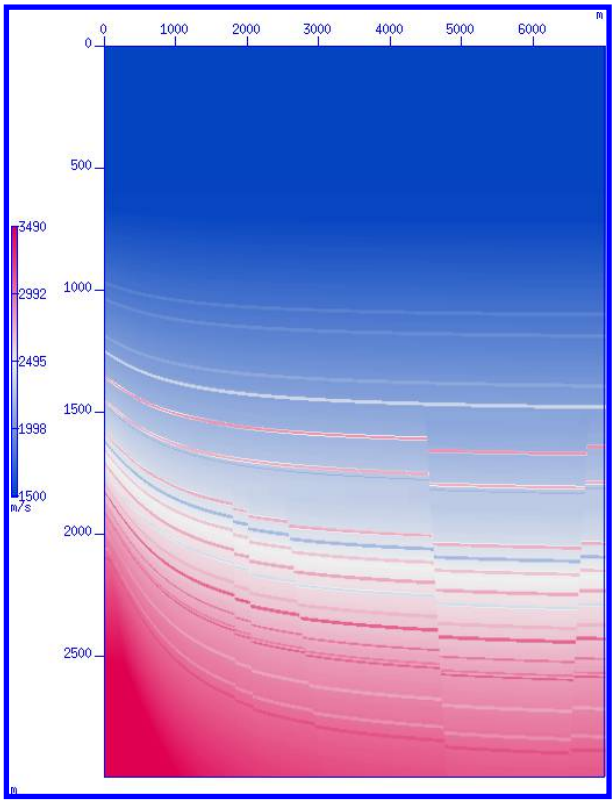

Figure 1: The true baseline velocity model. The true density model was obtained from the velocity by dividing it by 1500.

Both forward modeling and inversion are performed on a 700 (horizontal) by 600 (vertical) computational grid with a 10 m horizontal and 5 m vertical spacing. A Ricker wavelet centered at 10 Hz is used as a source, and absorbing boundary conditions are applied at the surface to avoid surface-related multiples. Two different streamer acquisition geometries are used for the baseline and monitor surveys with 39 shots and a 260 m shot spacing, with offsets ranging from 10 m to 7 km. The two surveys are shifted by 100 meters with respect to each other. Our starting velocity model was obtained from the true baseline model using a 400 m smoothing filter. We use frequency continuation from 10 to 30 Hz, with the maximum frequency for each experiment determined using the method of Sirgue and Pratt (2004). In each experiment we conduct a broadband (from 0 to the maximum frequency) time-domain full-waveform inversion to convergence, using the objective functions of Equations 1 and 2 at the first stage of the inversion, and Equations 3 and 4 at the second stage. We intentionally avoid density inversion in order to demonstrate the effect of amplitude errors on our 4D FWI.

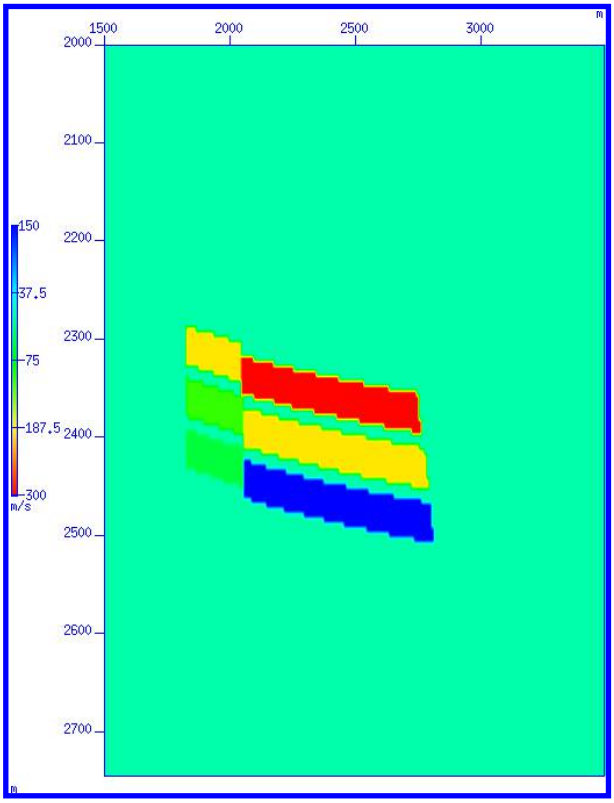

Figure 2: The true velocity change. The true density change was obtained from the velocity change by dividing it by 1500.

First, we conduct a parallel-difference FWI (Asnaashari et al., 2012) after adding random Gaussian noise to the data. The signal-to-noise ratio (SNR) peaked at about 10 dB, but deteriorated to 1 dB below 5 and above 24 Hz. Figure 3 shows the result of the parallel-difference FWI. The inversion produced oscillatory artifacts and quantitative errors that are evident both in Figure 3 and the well logs of Figures 5 and 6. The result of the first stage of our simultaneous regularized inversion is shown in Figure 4, and is in a good quantitative agreement with the true model difference—see Figures 5 and 6.

However, the blocky inverted model of Figure 4 has an obvious flaw: the TV-regularized inversion on our 5 m grid has removed the separation between the top two large compartments (see Figure 5) and the separation between any of the small compartments (see Figure 6). Although the effects on the

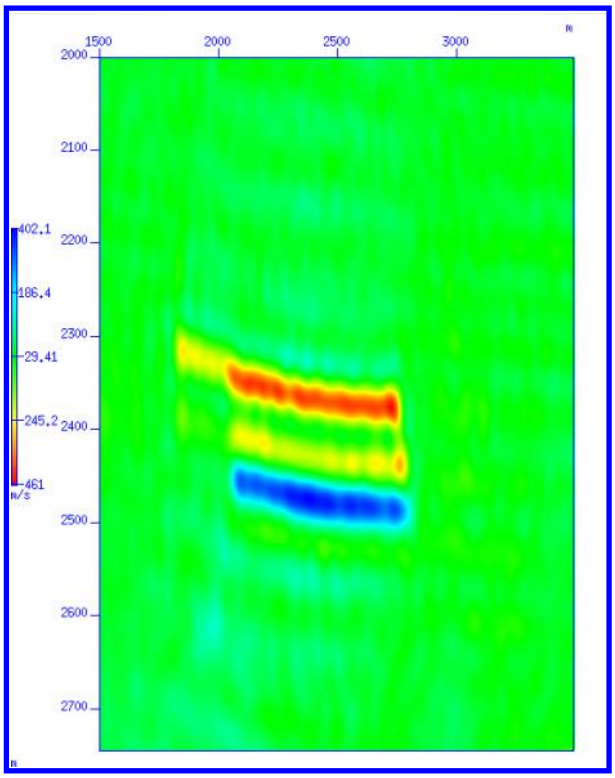

Figure 3: Velocity difference inverted using parallel-difference time-lapse FWI.

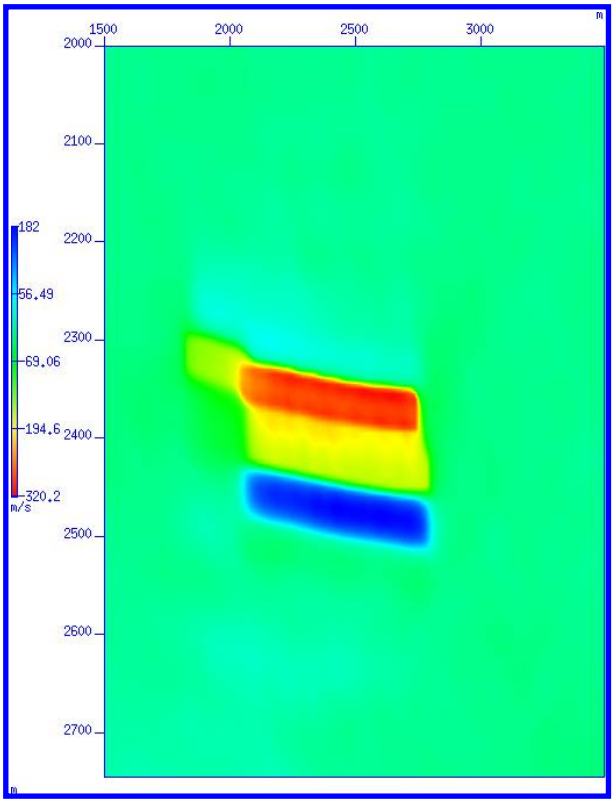

Figure 4: Velocity difference inverted at the first stage of the inversion using the normalized L_2 data misfit and a model-difference TV regularization.

travel times of the two ≈ 15 m-thick reservoir separation layers are small and ignored by the blockiness-promoting TV regularized inversion, the amplitude effects of the velocity model difference at the reservoir interfaces may be significant, and can be fitted by sparse and "spiky" diffractors at the reservoir boundaries.

Therefore, at the second stage of our cascaded inversion we minimize the standard L_2 misfit function with a sparsity-promoting L_1 model-difference regularization in Equations 3 and 4, setting Δm_0 equal to the model difference of Figure 4. The results of the cascaded inversion are shown in Figures 7 and 8. We now recover both separators for the large compartments and one separator for the small compartments without creating any additional oscillatory artifacts in comparison with the first stage of the inversion. The weakest and deepest of the negative velocity anomalies in the up-dip compartments is not well resolved by any inversion, apparently due to limited resolution. The model-difference amplitudes at reservoir boundaries are over-predicted in the second inversion because these now account for the effects of both velocity and density change. With the true density change chosen proportional to the true velocity change as described earlier, the neglected density has the effect of boosting the reflectivity, resulting in a leakage into the inverted velocity difference when the L_2 data misfit function of Equation 3 is used.

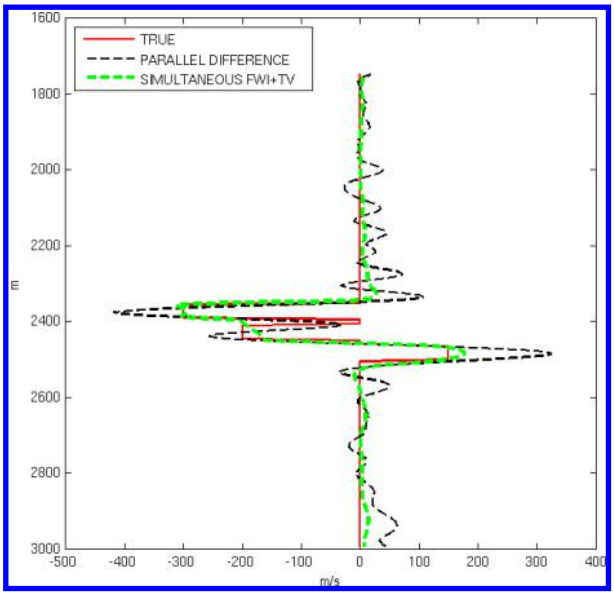

Figure 5: Model-difference logs at a 2.7 km inline coordinate showing the true (red), parallel-difference time-lapse FWI (black), and TV-regularized simultaneous time-lapse FWI (green) model differences.

CONCLUSIONS

The proposed cascaded multiscale 4D FWI method harnesses the power of various misfit functionals and regularization penalties to resolve subsurface model changes at various scales. A total-variation model-difference regularization helps to reduce oscillatory artifacts, but it may also penalize fine features of interest, especially when applied over coarse grids. An L_1 regularization, on the other hand, may penalize blocky features, leaving out important effects within the reservoir and overburden. However, a cascaded application of 4D FWI in combination with the TV seminorm and L_1 norm can separate traveltime and amplitude effects, and provide an imaging tool that complements the existing image-difference techniques.

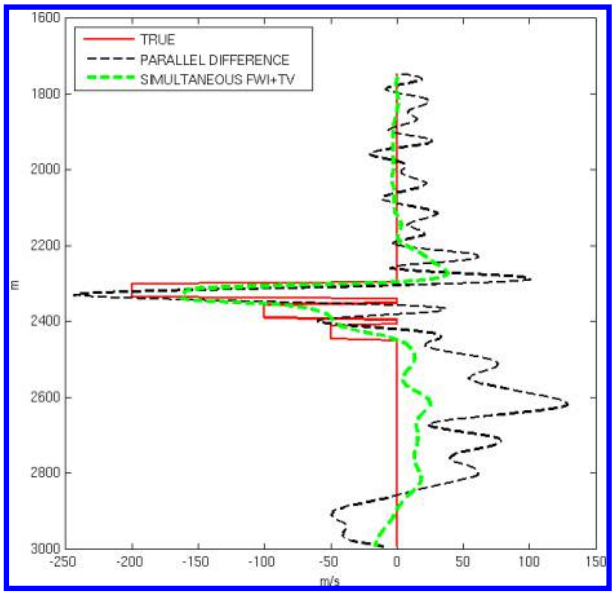

Figure 6: Model-difference logs at a 2 km inline coordinate showing the true (red), parallel-difference time-lapse FWI (black), and TV-regularized simultaneous time-lapse FWI (green) model differences.

ACKNOWLEDGMENTS

The authors would like to thank David Johnston, Biondo Biondi, Tom Dickens, Xinyou Lu, Gboyega Ayeni, Grant Gist, and Eric Wildermuth for a number of useful discussions, and ExxonMobil Upstream Research Company for the permission to publish this work.

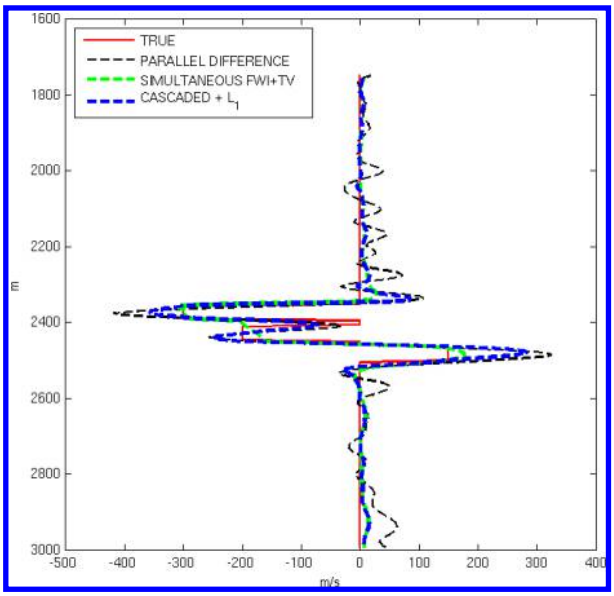

Figure 7: Model-difference logs at a 2.7 km inline coordinate showing the true (red), parallel-difference time-lapse FWI (black), TV-regularized simultaneous time-lapse FWI (green), and L_1-regularized cascaded time-lapse FWI (blue) model differences.

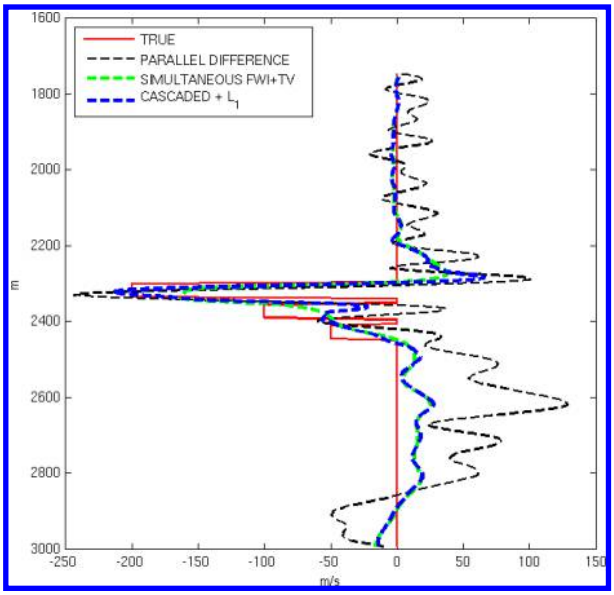

Figure 8: Model-difference logs at a 2 km inline coordinate showing the true (red), parallel-difference time-lapse FWI (black), TV-regularized simultaneous time-lapse FWI (green), and L_1-regularized cascaded time-lapse FWI (blue) model differences.

EDITED REFERENCES

Note: This reference list is a copyedited version of the reference list submitted by the author. Reference lists for the 2017 SEG Technical Program Expanded Abstracts have been copyedited so that references provided with the online metadata for each paper will achieve a high degree of linking to cited sources that appear on the Web.

REFERENCES

Alemie, W., and M. Sacchi, 2016, Joint reparametrized time-lapse full-waveform inversion: 86th Annual International Meeting, SEG, Expanded Abstracts, 1309–1314, http://dx.doi.org/10.1190/segam2016-13879371.1.

Asnaashari, A., R. Brossier, S. Garambois, F. Audebert, P. Thore, and J. Virieux, 2012, Time-lapse imaging using regularized FWI: A robustness study: 82nd Annual International Meeting, SEG, Expanded Abstracts, 1–5, http://dx.doi.org/10.1190/segam2012-0699.1.

Ayeni, G., 2011, Time-lapse seismic imaging by linearized joint inversion: Ph.D. thesis, Stanford University.

Ayeni, G., and B. Biondi, 2012, Time-lapse seismic imaging by linearized joint inversion — A Valhall Field case study: 82nd Annual International Meeting, SEG, Expanded Abstracts, 1–6, http://dx.doi.org/10.1190/segam2012-0903.1.

Girard, A., and I. Vasconcelos, 2010, Image-domain time-lapse inversion with extended images: 80th Annual International Meeting, SEG, Expanded Abstracts, 4200–4204, http://dx.doi.org/10.1190/1.3513744.

Johnston, D., 2013, Practical applications of time-lapse seismic data: SEG.

Maharramov, M., and U. Albertin, 2007, Localized image-difference wave-equation tomography: 77th Annual International Meeting, SEG, Expanded Abstracts, 3009–3013, http://dx.doi.org/10.1190/1.2793096.

Maharramov, M., and B. Biondi, 2014, Joint full-waveform inversion of time-lapse seismic data sets: 84th Annual International Meeting, SEG, Expanded Abstracts, 954–959, http://dx.doi.org/10.1190/segam2014-0962.1.

Maharramov, M., and B. L. Biondi, 2017, Full waveform inversion for reservoir monitoring — Pushing the limits of subsurface resolution: 79th Annual International Conference and Exhibition, EAGE, Extended Abstracts, We PRM 16, http://dx.doi.org/10.3997/2214-4609.201700025.

Maharramov, M., B. L. Biondi, and M. A. Meadows, 2016, Time-lapse inverse theory with applications: Geophysics, **81**, no. 6, R485–R501, http://dx.doi.org/10.1190/geo2016-0131.1.

Maharramov, M., B. Biondi, and S. Ronen, 2015, Robust simultaneous time-lapse full-waveform inversion with total-variation regularization of model difference: 77th Annual International Conference and Exhibition, EAGE, Extended Abstracts, We P3 09, http://dx.doi.org/10.3997/2214-4609.201413085.

Qu, S., and D. Verschuur, 2016, Getting accurate time-lapse information using geology-constrained simultaneous joint migration-inversion: 86th Annual International Meeting, SEG, Expanded Abstracts, 5451–5456, http://dx.doi.org/10.1190/segam2016-13964374.1.

Raknes, E., W. Weibull, and B. Arntsen, 2013, Time-lapse full waveform inversion: Synthetic and real data examples: 83rd Annual International Meeting, SEG, Expanded Abstracts, 944–948, http://dx.doi.org/10.1190/segam2013-0540.1.

Routh, P. S., J. R. Krebs, S. Lazaratos, A. I. Baumstein, I. Chikichev, N. Downey, D. Hinkley, and J. E. Anderson, 2011, Full-wavefield inversion of marine streamer data with the encoded simultaneous source method: 73rd Annual International Conference and Exhibition, EAGE, Extended Abstracts, F032, http://dx.doi.org/10.3997/2214-4609.20149730.

Routh, P., G. Palacharla, I. Chikichev, and S. Lazaratos, 2012, Full wavefield inversion of time-lapse data for improved imaging and reservoir characterization: 82nd Annual International Meeting, SEG, Expanded Abstracts, 1–6, http://dx.doi.org/10.1190/segam2012-1043.1.

Shragge, J., and D. Lumley, 2013, Time-lapse wave-equation migration velocity analysis: ASEG Extended Abstracts 2012: 22nd Geophysical Conference, 1–5, http://dx.doi.org/10.1071/ASEG2012ab197.

Sirgue, L., and R. Pratt, 2004, Efficient waveform inversion and imaging: A strategy for selecting temporal frequencies: Geophysics, **69**, 231–248, http://dx.doi.org/10.1190/1.1649391.

Willemsen, B., and A. Malcolm, 2015, Regularizing velocity differences in time-lapse FWI using gradient mismatch information: 85th Annual International Meeting, SEG, Expanded Abstracts, 5384–5388, http://dx.doi.org/10.1190/segam2015-5908610.1.

Yang, D., A. E. Malcolm, and M. C. Fehler, 2014, Time-lapse full waveform inversion and uncertainty analysis with different survey geometries: 76th A Annual International Conference and Exhibition, EAGE, Extended Abstracts, We ELI1 10, http://dx.doi.org/10.3997/2214-4609.20141120.

Zheng, Y., P. Barton, and S. Singh, 2011, Strategies for elastic full waveform inversion of timelapse ocean bottom cable (OBC) seismic data: 81st Annual International Meeting, SEG, Expanded Abstracts, 4195–4200, http://dx.doi.org/10.1190/1.3628083.